Surface & Coatings Technology 485 (2024) 130915

Contents lists available at ScienceDirect

Surface & Coatings Technology

journal homepage: www.elsevier.com/locate/surfcoat

Full Length Article

Effect of titanium and deposition parameters on microstructure and mechanical properties of W-Ti-B thin films deposited by High Power Impulse Magnetron Sputtering

Tomasz Mościcki [a,*], Rafał Psiuk [a], Dariusz Jarząbek [a,c], Marta Ciemiorek-Bartkowska [b], Krzysztof Kulikowski [b], Jarosław Jasiński [d], Mateusz Włoczewski [b], Małgorzata Lewandowska [b]

[a] Institute of Fundamental Technological Research, Polish Academy of Sciences, Pawinskiego 5B, 02-106 Warsaw, Poland
[b] Faculty of Materials Science and Engineering, Warsaw University of Technology, Wołoska 141, Warsaw 02-507, Poland
[c] Faculty of Mechatronics, Warsaw University of Technology, Boboli 8, 02-525 Warsaw, Poland
[d] NOMATEN Centre of Excellence, National Centre for Nuclear Research, A. Soltana 7, 05-400 Otwock, Poland

ARTICLE INFO

Keywords:
Ternary transition metal diboride thin films
Mechanical properties
HiPIMS magnetron sputtering
Wear resistance and adhesion

ABSTRACT

Tungsten diboride alloyed with transition metals provides an opportunity to obtain exceptional mechanical, physical, and chemical properties. We report a strategy for designing and synthesizing of superhard and low-compressible ceramic thin films with increased toughness and lowered residual stresses ($\sigma < -0.9$ GPa) deposited with high-power impulse magnetron sputtering (HiPIMS) from one target. The addition of 7–12 % titanium promotes additional strengthening mechanisms of the layers in one material, leading to the improvement of wear resistance compared to an alloyed WB_{2-z} yet at even higher hardness 43.8 ± 2.1 GPa and nanoindentation toughness 4.9 ± 0.2 MPa$\sqrt{m}$. The compression of the micropillar shows that titanium addition changed the type of nanoindentation from cracking along the slip plane to bulging on the top of the pillar and next the crack initiation along column boundaries. The highest adhesion of the layers is obtained for addition of 7 % titanium and in all cases the wear has abrasive character. The controlled use of 200 μs pulses during synthesis with HiPIMS allows for an increase in the deposition rate and maintaining exceptional mechanical properties of the layers even at a substrate temperature of 300 °C.

1. Introduction

The design and processing of very hard but yet ductile materials are paramount to new technologies for extreme environments like space or nuclear fusion power plants [1,2]. However, the strength and high toughness of currently developed engineering materials are commonly conflicting [3]. Over the past years, ternary nitrides, carbides, and borides have drawn great attention as they open a new branch of compositional possibilities for designing innovative materials with unique properties. While nitrides [4] and carbides [5] are already quite well recognized, borides require further research [6–8].

One example of strong and yet ductile materials is superhard (H > 40 GPa) ternary transition metal diboride coatings deposited primarily with the magnetron sputtering method [7]. It is necessary to underline that the coatings made of those materials, in additionally to excellent mechanical properties, can possess also other unique functional and physical properties as a thermal stability and oxidation resistance at temperatures even above 1000 °C [9,10] Therefore, the development of hard and durable tungsten borides layers alloyed with other transition metal like tantalum [11,12], chromium [13,14] or zirconium [15] and improvement of their deposition method have been a theme of recent articles [16,17].

The first-principles theoretical calculations showed that the α/α-type TiB_2/WB_2 is one of the promising candidates providing the atomic-scale basis for enhanced toughness and resistance to crack growth while maintaining high hardness [6,8,18]. However, as studied by Sobol et al. [19] the magnetron-sputtered W-Ti-B compounds (content of titanium below 10 % at. concerning tungsten) possessed properties different than those predicted by theoretical calculations. Deposited with DC magnetron sputtering coatings were composed mainly of β-WB phase with an orthorhombic crystal lattice. However, even a very low content of Ti (about 0.6 at.%) stimulated the formation of α-(Ti,W)B_2 phases with a

* Corresponding author.
E-mail address: tmosc@ippt.pan.pl (T. Mościcki).

https://doi.org/10.1016/j.surfcoat.2024.130915
Received 15 April 2024; Received in revised form 10 May 2024; Accepted 12 May 2024
Available online 14 May 2024

hexagonal crystal lattice. Further increasing of titanium to 10 % at. led to obtain the coatings with hardness H = 33 GPa and H/E = 0.082 respectively. Additionally, to obtain α-(Ti,W)B_2 phase a very high substrate temperature (700 °C) was needed. Moscicki et al. [20] tried to resolve this problem by using RF magnetron sputtering of targets with over stoichiometric boron ($W_{1-x}Ti_xB_{4.5}$) at substrate temperature 520 °C. The introduction of titanium and the grater energy of the particle depositing on the substrate resulted in the use of RF against DC generator causing the change of microstructure and the metastable hexagonal α-(W,Ti)B_2 phase. In this case, the hardness of the coatings was 39.2 ± 1.5 GPa, and the plasticity index (H/E*) was above 0.1. Authors also claimed that with the applied deposition conditions, i.e. argon pressure p_{Ar} = 0.9 Pa, substrate temperature T_s = 520 °C (where the melting temperature T_m of WB_2 = 2365 °C) during RF magnetron sputtering films without titanium with "ZONE 1" microstructure and columnar crystallites separated by voids were formed. The addition of titanium caused the increase of the *Ts/Tm* ratio due to the lowering of melting temperature of (W,Ti)B_2 and probably the change of stress state to the compressive. However, the microstructure or even stress value was not presented.

Further increase of mechanical properties of deposited films can be obtained by the increase of energy and higher ionization of deposited material [21]. Chrzanowska et al. [22] proposed the hybrid method of W-Ti-B coatings deposition to fulfil this assumption. Magnetron sputtering combined with pulsed laser deposition (MSPLD) has advantages like an additional source of ionization (laser), and abrupt vaporization of the target during ablation, giving high kinetic energy particles. As a result the coatings deposited from W_2B_5 (MS) and pure titanium (PLD) targets at a substrate temperature of 520 °C were crystalline with a dominant α-WB_2 phase. The coatings deposited with an addition of 5.5 % at. Ti were superhard with a hardness of 65 ± 8.2 GPa (load 2mN) and exhibited effective Young's modulus E^* = 510 ± 12.3 GPa values. The hybrid MSPLD method allowed to obtain very good mechanical properties but also possessed disadvantages like the low rate of deposition, high roughness and was quite complicated to synthesize compared to other presented methods.

The above research shows that to obtain the properties of the layers resulting from theoretical calculations, it is necessary to use two strategies: (I) increasing the energy and ionization of the arriving particles to increase the surface diffusion of adatoms and reduce the deposition temperature, (II) selecting and addition of the appropriate amount of alloying element.

In the first strategy, high energies enhance the reinforcement of the films. The increased mechanical properties resulting from high-energy sputtering are the effects of reduced intra-column gaps and a more rigid structure of the layers. The higher fluence of ionized particles increases surface diffusion and impact, resulting in stronger nanocolumnar bonding [23]. Additionally, the deposition process, thanks to the addition of energy from particles bombarding thin layers, can be carried out at lower substrate temperatures. As a result of this additional energy, atoms on the substrate surface can move more freely on the surface, resulting in a stable film microstructure at lower substrate temperatures [21,24].

Regarding the second strategy, transition metal borides benefit profoundly from solid solution strengthening [25]. This is due to the fact that alloying elements lead to much higher lattice distortions than substitutional elements, which strongly affect their interaction with dislocations. The alloying element is able to form a substitutional solid solution with WB_x with a solubility limit of <20 at. % for Ti and metal atom substitution causes intrinsic hardening [26]. Further increasing of additional transition metal content influences extrinsic hardening through grain morphology refinement and the precipitation of secondary phases. Moreover, additives can also promote or inhibit the structure forming process [27]. In the case of magnetron sputtered micro- or nanostructured thin films, the overall microstructural domain size decreases. Therefore, it is evident that the increased share of grain boundaries, interphase boundaries, and free surfaces influences the strengthening mechanisms of the governing system. These features further restrict dislocation sources' availability, activity, and mutual interactions [28].

In this article, tungsten boride coatings alloyed with different amounts of titanium (strategy two) are deposited from a single sputtering target with High Power Impulse Magnetron Sputtering (HiPIMS). HiPIMS technique utilizes exceptionally high power densities of the order of kW/cm^2 in short pulses of tens of microseconds at low duty cycle (on/off time ratio) of <15 % [29], which fulfils the first strategy. The possibility of obtaining superhard yet ductile coatings at rationally low substrate temperatures (below 300 °C) was proven with micromechanical measurement methods. Additionally, the wear resistance of films and adhesion to nitrided stainless steel substrate were compared for different amounts of titanium.

2. Experimental procedures and methods

2.1. Deposition of the layers – High Power Impulse Magnetron Sputtering (HiPIMS)

Sputtering targets were prepared from pure elements using the spark plasma sintering (SPS) technique. Powders of Ti (99.8 % purity, average grain size 250–350 μm), W (99.9 % purity, grain size 25 μm, Sigma Aldrich), and B (95 % purity, average grain size 1 μm) in a (W_{1-x} + Ti_x)/B (where x = 0; 0.08; 0.16; 0.24) molar ratio of 1/2.5 were mixed mechanically and SPS sintered. Detailed information on the manufacturing process has been described earlier in the literature [14]. Layers were deposited in a vacuum chamber that was pumped down to a base pressure of 4 × 10^{-8} mbar and then filled with argon to a working pressure of 0.9 Pa. A two-inch diameter target was sputtered using a PREVAC MS2 63C1 magnetron device with a HiPIMS power supply. The pulse parameters were following: average input power 250 W, frequency 700 Hz and pulse duration 20 and 200 μs (according to Table 1). The negative DC substrate potential of 50 V was applied to the substrate.

Sputtered material was deposited on a Si (100) substrate (ITME, Poland) for structure and mechanical properties analysis and on an ion-nitrided steel QRO90 for wear resistance and adhesion testing. Substrates were placed in front of the magnetron cathode at 80 mm from its surface. Before sputtering, the substrate surface was plasma cleaned by applying a −800 V bias voltage for 15 min. During deposition, the substrate was heated to 300–400 °C (Table 1). The resistive substrate heater (refractory metal module with a silicon carbide-coated graphite (SiCg) heating element) was placed on the backside of the substrate. The distance from the heater to the substrate was 10 mm. Each coating was deposited for 90 min. The thickness of the obtained specimens is presented in Table 1.

2.2. Microstructural characterization, phase analysis and composition

Surface morphology and film cross-section were evaluated using the Hitachi Su-70 scanning electron microscope. Cross sections were acquired by applying pressure on the Si plate using side cutters, which led

Table 1
Chemical composition of the sputtered W-Ti-B targets, HiPIMS deposition parameters and measured thickness.

Target chemical composition	Substrate temperature [°C]	Pulse duration [μs]	Thickness [μm]
WB2.5	400	200	2.09 ± 0.01
W0.92Ti0.08B2.5	400	200	1.88 ± 0.02
W0.84Ti0.16B2.5	400	200	1.75 ± 0.01
W0.76Ti0.24B2.5	400	200	1.72 ± 0.02
W0.76Ti0.24B2.5	350	200	1.84 ± 0.01
W0.76Ti0.24B2.5	350	20	1.19 ± 0.03
W0.76Ti0.24B2.5	300	200	1.57 ± 0.01

to the plate's fracture. Specimens for surface and cross-section observations were mounted directly to the SEM table using carbon adhesive, to provide proper conductivity.

The thickness of the films was measured based on SEM images (Table 1). Phase analysis was conducted with XRD examination at room temperature using Bruker D8 ADVANCE X-ray diffractometer with filtered Cu Kα radiation (λ = 0.154056 nm). The measurements were carried out at a constant angle of incidence of the primary beam Θ - 2°. The recording conditions were as follows: voltage - 40 kV, current - 40 mA, angle range 2Θ - 20° to 110°, step $\Delta 2\Theta$ - 0.025°, counting time - 5 s. The chemical composition of the layers was measured using an energy dispersive X-ray spectroscopy (EDS). The analysis of light elements, such as boron, especially in the presence of heavy elements, is subject to significant measurement error [30]. Therefore, before determining the composition of the layers, the EDS detector was calibrated with a commercial W_2B_5 reference sample (purity of 99.9 %, TYR Material, China). According to [31], the more precise results for boron content measured with EDS are obtained with lower accelerating voltage. The results of composition measurement with 7 kV and 10 kV voltage do not differ significantly (the statistical errors (uncertainty) of the measurement is lower than 8 %), therefore, in article, results for 10 kV accelerating voltage are considered.

2.3. Mechanical properties

Mechanical properties of the W-Ti-B layers were evaluated with nanoindentation test and compression of microopillars. Nanoindentation was carried out using Berkovich indenter on Vantage Alpha by Micromaterials nanohardness tester. The displacement of the indenter as a function of the load was recorded, on which nanohardness and reduced Young's modulus were determined according to the Oliver-Pharr method, which considers the current geometry of the indenter resulting from operational wear. For hardness measurement a load of 10 mN was used, with a load boost time of 10 s, load shedding time of 10 s and dwell period of 5 s. After each nanoindentation measurement at the final load did not exceed 10 % of the nominal measurement load, an analysis of the thermal drift of the material was carried out for 5 s. On each element, 25 measurements were made in a 5 × 5 grid. The maximum penetration depth does not exceed 10 % of the layer thickness. The elastic modulus is more sensitive to the effect of substrate, therefore was designated with loads 2 mN.

Nanoindentation toughness measurement was performed in-situ using an Alemnis Nanoindenter equipped with a cube corner tip. The experiments were carried out with two different maximum loads F_m – 200 nN and 300 nN. The formula used to determine the nanoindentation toughness of brittle materials was [32]:

$$K_{IC} = \delta\left(\frac{E}{H}\right)^{1/2}\frac{F_m}{c^{3/2}}$$

After the tests, the imprints were imaged with the use of SEM (Zeiss Crossbeam 350), and the average crack lengths were precisely measured. The elastic modulus E and hardness H were also measured and determined by nanoindentation using Berkovich indenter (mentioned above in the section).

δ is an empirical constant, dependent on indenter shape and extracted from reliable sources in the literature [33]. For the cube-corner indenter used, a value of 0.036 was assumed.

The in-plane residual stresses of $W_{1-x}Ti_xB_y$ thin films are obtained using the modified Stoney equation by determining the substrate (diameter 3 in.; Si (111)) wafer curvature from scanning profilometer (Hommel Etamic T8000) measurements. More details are provided in reference [34].

The yield strength and ultimate compression strength were measured by micro-pillar compression. Micropillars on each sample were fabricated using a Focused Ion Beam (FIB, Zeiss Crossbeam 350). The general flow of the process was to mill rings in the material, each starting at the outer diameter and milling toward the centre. Milling was done in three steps: coarse (30 kV, 3 nA), slow (30 kV, 200 pA), and precise (30 kV, 2 pA). The target diameter of the pillar was 800 nm. After fabrication, each pillar was imaged with SEM to measure the pillar diameter and height. The actual height of the pillars was calculated, considering the angle at which the SEM image was taken. Next, the pillars were compressed using in-situ Alemnis Nanoindenter, and the image after compression was recorded. For each sample, 3 pillars were produced and examined. The data for each pillar was analyzed using the exact dimensions measured with SEM (Zeiss Crossbeam 350).

2.4. Tribology and adhesion testing

Wear resistance and adhesion measurements were performed for layers deposited on Q900 steel elements with a 15 mm diameter and 5 mm thickness. Wear resistance measurements were carried out on the T-21 tribotester manufactured by ITEE RADOM using the “ball-on-disc” method, in which a stationary alumina ball of 6.35 mm (1/4 in.) diameter (class G28), acting as counter-sample, was mounted on a rigid arm and is in contact with the surface of a rotating sample in the form of a disc. During the test, a force tangential to the sample movement path was recorded, corresponding to the movement resistance in the ball-disc tribological system. Measurements were carried out without external lubricants at ambient temperature (22 ± 3 °C). The following test parameters were used to determine the coefficients of friction: friction node load of 5 N, 5000 revolutions, linear speed of 0.1 m/s, track radius of 5 mm and friction distance of 157 m. Additionally, samples after the wear test were subjected to surface roughness measurements using a Sensofar Tech Industries interferometric profilometer. An abrasion cross-section profile was determined, based on which the index of volumetric wear of the material Wv was calculated. Before the test, the surface of the PVD coating and the counter-sample was degreased in acetone (PA). Before and after the test, disc mass measurements were carried out to determine the loss of abrasive material. After each test, the sample surface was observed on a Nikon Eclipse LV150N light microscope using polarized light.

The layers adhesion and critical forces tests were carried out on the CSM Scratch-test device, which scratches the material's surface using an indenter with a defined blade geometry. The tested sample was moved at a constant speed in the direction perpendicular to the blade, which, pressed against the surface with a given pressure, penetrated the material. During the test, the pressure force, friction force, blade penetration depth and the acoustic emission signal related to layer cracking and decohesion effect were recorded. The tests were carried out using a Rockwell diamond indenter with a radius of 0.2 mm as a counter-sample, scratch length of 8 mm and linearly variable pressure force from 1 to 20 N. The analysis of the adhesion of the tested layer was carried out based on the analysis of the course of the recorded parameters in correlation with microscopic observations of the resulting crack realized on a Nikon Eclipse LV150N light microscope.

3. Results

3.1. Surface and cross-section analysis

3.1.1. Effect of Ti content

The measured amount of film compositions concerning target composition are presented in Fig. 1. Both titanium and boron amounts are understoichiometric. A very low amount of boron compared to the composition of WB_2 confirms the presence of vacancies. However, as DFT theoretical calculations show, the introduction of vacancies has a positive effect on the mechanical properties of the deposited films [18]. Considering the measurement errors, the amount of boron is independent of the target composition. In the case of titanium, the difference between the amount of this element in the target and the deposited film

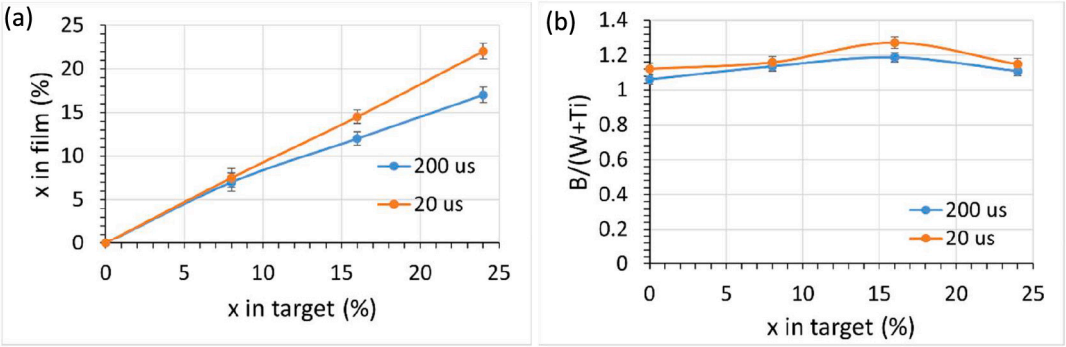

Fig. 1. Change of titanium (a) and boron (b) content in the function of pulse duration and target composition (EDS), x – the amount of titanium to tungsten (Ts = 400 °C, τ = 200 μs).

rises as its amount in the target increases. For example, for the $W_{0.92}Ti_{0.08}B_{2.5}$ target, the difference is about 7 %, while for the $W_{0.76}Ti_{0.24}B_{2.5}$ target, it is 19 % (pulse duration τ = 200 μs). As presented in Fig. 1, more boron and titanium are deposited with a shorter pulse duration. Using 20 μs pulse duration increases peak power and causes greater ionization of sputtered material. This effect is even a more significant attraction of ionized material to the substrate where the bias is used. Due to the significant differences in the composition of the films with the sputtered targets, in the further part of the article, the properties of the coatings will be presented in relation to the actual amount of titanium in the films. Additionally, due to possible errors in determining the amount of boron [30], instead of its exact content, the B_{2-z} notation will be used.

The fracture surface and plan-view of layers containing 0 %; 7 %; 12 % and 17 % at. of Ti, respectively, deposited at 400 °C and τ = 200 μs are shown in Fig. 2(a-h). No pores, cracks or voids were observed on the obtained films. The sample without Ti addition is characterized by a featureless microstructure, which is visible on its cross-section.

This is also confirmed by XRD analysis, as no distinct peaks are visible for WB_2, as shown in Fig. 3. The addition of Ti results in acquiring a crystalline structure, which is visible on fracture surface images as a columnar structure mainly perpendicular to the substrate surface, along which a fracture was created. The fracture surface is rough and geometrically defined. The crystalline phases were identified as α-WB_2 and α-TiB_2. Both phases are hexagonal (*P6/mmm*), however in the case α-WB_2, this polymorph is metastable and can be obtained when the metallic or boron vacancies are present [12]. In the case of this phase, the diffraction peaks are shifted toward lower angles, which indicates a changing of lattice parameters of the phase due to the incorporation of

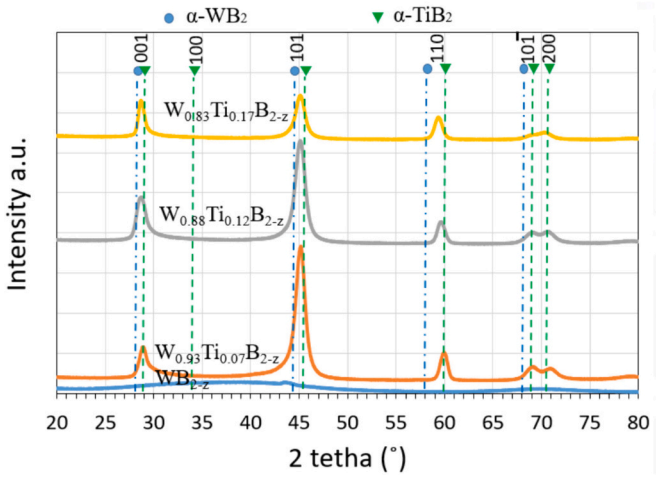

Fig. 3. X-ray diffraction pattern of $W_{1-x}Ti_xB_{2-z}$ layers with increasing Ti content (0 < x < 0.20). Lattice parameters: α-WB2 a = 3.026 Å c = 3.087 Å; α-TiB2 a = 3.033 Å, c = 3.231 Å (Ts = 400 °C, τ = 200 μs)

the titanium into the crystal lattice of the material (c = 3.087 Å for 0 % to c = 3.107 Å for 17 % at. Ti addition). Moreover, the peaks are broadened, indicating the film's fine-crystalline (nanocrystalline) structure. The calculated from the XRD pattern crystallite size (Scherrer formulae) is 13–19 nm for 7 % and 16 % of titanium, respectively. For samples sputtered from targets with 16 % and 24 % Ti content, the columnar structure is visible throughout the thickness of the sample,

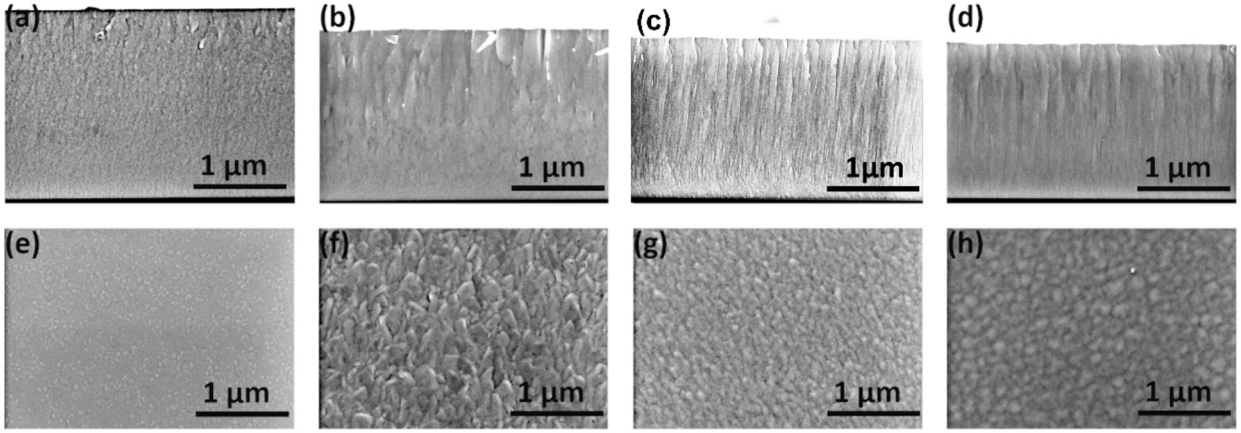

Fig. 2. Cross-sections (a-d) and surface morphology (e-h) of W-Ti-B layers deposited on Si substrate sputtered from 0 %; 8 %; 16 % and 24 % of Ti content targets (Ts = 400 °C, τ = 200 μs).

whereas in the sample with 7 % at. Ti, such structure is visible at approximately the upper half of the film. It is worth noticing that columns visible in the sample sputtered from the target with 16 % Ti content are composed of V-shaped grains near the substrate surface and columnar in the film's upper part. Differences between samples with and without Ti are also visible on the surface, as shown in the SEM images in Fig. 2(e-h). The surface of the WB_{2-z} sample is smooth, while the rest feature rough morphology with a feather-like shape (Fig. 2f) or granules (Fig. 2g,h), characteristic of columnar structures with visible boundaries.

3.1.2. Effect of deposition parameters

Fig. 4 shows SEM images of the fracture surface and plan-view of films deposited from the target with 24 % Ti content deposited at substrate temperatures T_s of 400 °C, 350 °C and 300 °C and pulse duration τ of 200 μs and, for comparison, 20 μs. Decreasing substrate temperature does not have a considerable impact on the morphology. Only a slight increase in surface roughness, as shown in Fig. 4b, d and h, can be observed, also demonstrated as more clearly geometrically defined fracture surfaces. A more noticeable effect is observed for decreasing pulse duration (compare Fig. 4c-d and e-f). With decreasing impulse length, layer thickness was reduced from 1.84 ± 0.01 μm to 1.19 ± 0.03 μm. Changes are also visible in roughness, which was reduced for film deposited using 20 μs pulse duration. Comparing Figs. 2c,g and 4e,f shows that a similar microstructure can be obtained by lowering the deposition temperature from 400 to 350 °C while shortening the pulse length (increase in the maximum power in the pulse) from 200 to 20 μs.

Lowering the deposition temperature to 300 °C did not cause significant changes in hardness and reduced Young's modulus. The obtained plastic index H/E^* (for comparison, see next section) for T_s = 350 °C is 0.117 and 0.110 for T_s = 300 °C. In the case of a shorter pulse duration of 20 μs the obtained reduced Young's modulus has the lowest value of 371.8 ± 28.5 GPa, and high hardness of 43 ± 3 GPa. However, because of the much lower deposition rate in the case of 20 μs, films deposited with pulse duration 200 μs were chosen for further investigation.

3.2. Mechanical properties

The nanohardness and reduced Young's modulus E^* of layers deposited at 400 °C as a function of Ti content is presented in Fig. a. The addition of Ti increases hardness by approximately 50 %, reaching up to 43.8 GPa for films with 17 % Ti. Similarly, E^* increases from 325 GPa to 405 GPa for samples with 7 % Ti content and does not change with higher titanium amount. Such a relation of both properties causes the rise of plastic work above 0.1. Presented in Fig. 5b elastic recovery W_e after titanium addition is above 0.6, which confirms the increase of film toughness [35].

The residual compressive stresses obtained by measuring the curvature of coated Si (111) substrates with alloyed coatings show no dependence on the Ti content (σ between −886 ± 120 and −1010 ± 87 MPa, Table 2). The growth morphology of coatings with titanium is also somewhat similar (with comparable column sizes (Fig. 2)). The dominating strengthening mechanism can be related to solid solution hardening effects, which include parelastic and dielastic contributions as TiB_2 and WB_2 have different lattice parameters and shear moduli [7]. In the case of WB_{2-z} the residual compressive stress is much lower due to lack of columnar structure.

The nanoindentation toughness values K_{Ic}, based on crack lengths with examples of cube-corner indents with load 300 mN, are presented in Fig. 6. The addition of Ti increases K_{IC}, but only for minor Ti contents. The film without titanium has an average length of radial cracks C_m of 2023 ± 182 nm, and the pile-up effect [13] can be observed around the induced nanoindentation impressions. For 7 % and 12 % Ti, cracks are shorter, and chipping is present around the indents. Further increasing the amount of titanium causes the elongation of cracks and lowers the chipping effect. Differences in crack propagation are also noticeable in Fig.6(b-d). For the samples without adding Ti, the cracks are straight and start ideally at the corners of the indents. The cracks for the Ti-added samples propagate in a variable direction, and the main crack sometimes does not occur at the corner of the indents. The shorter radial cracks are directly related to the higher compressive strain in samples with 7 % and 12 % Ti but also different microstructure of deposited films. Change from featureless to columnar and dense morphology and increased compressive stress cause cracks to propagate only under higher loads. For coating with 7 % titanium at a load 200 mN cracks are not visible, and determination of nanoindentation toughness is practically impossible. In the case of films without titanium cracks are short but measurable (Fig. 7). Detailed values of indentation and stress measurement results are listed in Table 2.

The values of the 0.2 % offset yield and ultimate compression strength from micro-pillar compression are presented in Fig. 8. Generally, with increasing Ti content, the compressive strength increases. The only exception is for 7 % Ti content material, which is weaker than for coating without titanium. Although these materials are as brittle as ceramics, there is a small range of plastic deformation, so for this reason, the 0.2 % offset yield strength was also determined. It is worth noting that for the sample with 17 % Ti, the offset yield point and ultimate compression strength values are very close. This sample fractured instantly when the elastic deformation ended. The 17 % Ti content

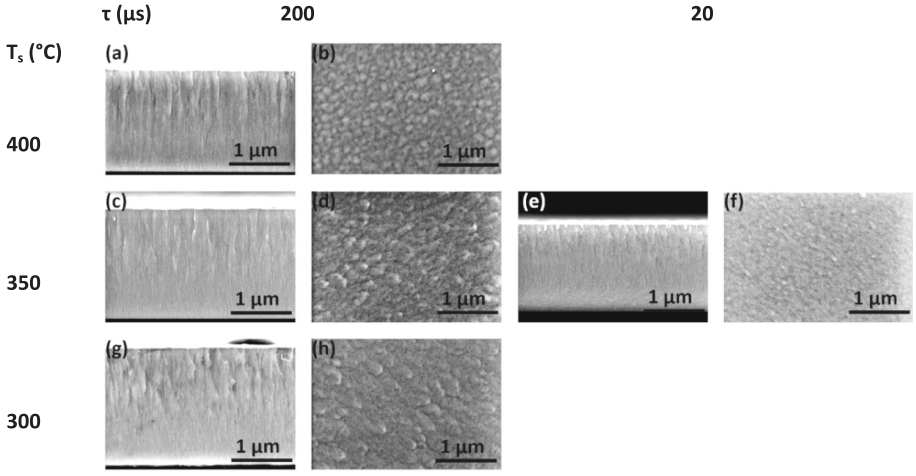

Fig. 4. Effect of different processing parameters on section structure and surface morphology of W-Ti-B layers deposited with HiPIMS using x = 24 % Ti target with τ = 200 μs at: 400 °C (a, b); 350 °C (c, d); 300 °C (g, h), and τ = 20 μs at 350 °C (e, f).

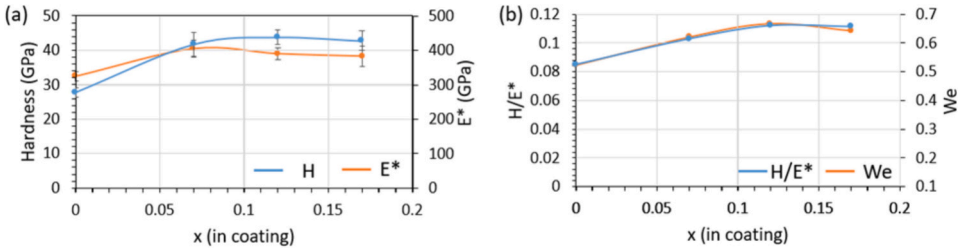

Fig. 5. Hardness and reduced Young's modulus (a) and plasticity index H/E* with elastic recovery (b) in a function of x (Ti content) in the $W_{1-x}Ti_xB_{2-z}$ lcoatings; Ts = 400 °C; τ = 200 μs.

Table 2
Hardness, reduced Young's modulus, nanoindentation toughness K_{IC} and residual stress of the W-Ti-B layers with various Ti content; T_s = 400 °C.

Sample	*H* [GPa]	*E** [GPa]	K_{IC} [MPa$\sqrt{m}$]	*σ* [MPa]
WB_{2-z}	27.7 ± 1.3	325 ± 13	3.8 ± 0.1	313 ± 95
$W_{0.93}Ti_{0.07}B_{2-z}$	41.7 ± 3.4	405 ± 26	5.0 ± 0.3	904 ± 60
$W_{0.88}Ti_{0.12}B_{2-z}$	43.8 ± 2.1	390 ± 18	4.9 ± 0.2	886 ± 120
$W_{0.83}Ti_{0.17}B_{2-z}$	42.7 ± 2.8	383 ± 29	3.7 ± 0.1	1010 ± 87

sample is the most brittle, which was confirmed by cube-corner nanoindentation toughness tests. SEM images of micro-pillars after compression presented in Fig. 8(b-e) show different fracture shapes for WB_{2-z} sample. A shear event oriented at ~30° angle concerning the pillar axis is visible (Fig. 8b). Such shear can facilitate the identification of the active slip systems in the featureless materials. The SEM images of the compressed pillars of alloyed coatings show uniform compression and bulging on the top of pillar and next the fracture along the column's axis, which is parallel to what was observed in Fig. 2b-d columnar grains and corresponded to {101} direction (Fig. 3).

3.3. Adhesion and tribology

Changes in friction force and penetration depth during the scratch test content are presented in Fig. 9. The tested coatings are characterized by high stability in the load range from 1 N to critical load L_{C3} loads (Fig. 9b), leading to delamination of the layers. In this load range, only surface distortion related to abrasive wear or plastic deformation of the substrate was observed, without damage as longitudinal or transverse cracks in the area of the wear track. In the case of the coating without the addition of titanium, an increased level of acoustic emission was already recorded from the initial force of 1 N due to the pores and/or inclusions on its surface. However, the interaction of the indenter with the surface did not lead to the formation of damage observable under an optical microscope at magnifications up to 1000×. As shown in Fig. 9b, the first recorded damage to the tested coatings was related to their delamination from the substrate (critical load L_{C3}), and occurred in the range of forces from 10.5 N (coating with 17 % Ti) to 13.4 N (7 % Ti). After exceeding the critical load L_{C3}, the coating underwent continuous, complete delamination during interaction with the indenter, which was recorded as sudden changes in acoustic emission, friction coefficient and penetration depth (Fig. 9a).

Depending on the Ti content in the layers, a change in the type of the initial delamination was observed. In the case of a WB_{2-z} coating, the chipping of the layer covers the area immediately in front of the indenter (Fig. 10). In the layer with the addition of 7 % titanium, delamination in the area on both sides of the crack is observed, which indicates a more vital transfer of stresses from friction force through the layer to its adjacent areas. A further increase in titanium content leads to layer delamination on the sides of the abrasion trace behind the indenter. Delamination, in this case, occurs during the tensioning of the coating. This mechanism indicates an increase in the tensile strength of the coating with an increase in Ti content, which allows the transfer of stresses exceeding the adhesion of the layers to the substrate.

The values of the friction coefficient, which was calculated as a quotient of frictional force to force of the pressure of the ball on the disc, are presented in Fig. 11a. The addition of Ti decreases the friction coefficient of the layers, except for film with 17 % Ti content (200 μs) where the similar value to 0 % Ti layer was obtained (~0.55). For comparison, when the deposition energy is increased by the shortening of pulse duration (20 μs) the layers are more dense and the surface less rough (see Fig.4e-f), which causes the friction coefficient to decrease for the same amount of titanium to 0.38. Similar and at the same time, the lowest values of the friction coefficient ~ 0.35 were obtained for the 7 % titanium W-Ti-B layer.

In Fig. 11b the wear rate for films with different Ti alloying is presented. During the "ball-on-disc" wear resistance test under a load of 5 N in 5000 cycles, only the WB_{2-z} coating was worn to the substrate after approximately 3300 revolutions. The wear rate for the sample with 0 % Ti is $25.76 \cdot 10^{-6}$ mm^3/Nm, which is approximately 10 times larger than the highest presented value obtained for the sample with 17 % Ti content deposited with τ = 20 μs (Fig. 11d). The lowest value of wear rate

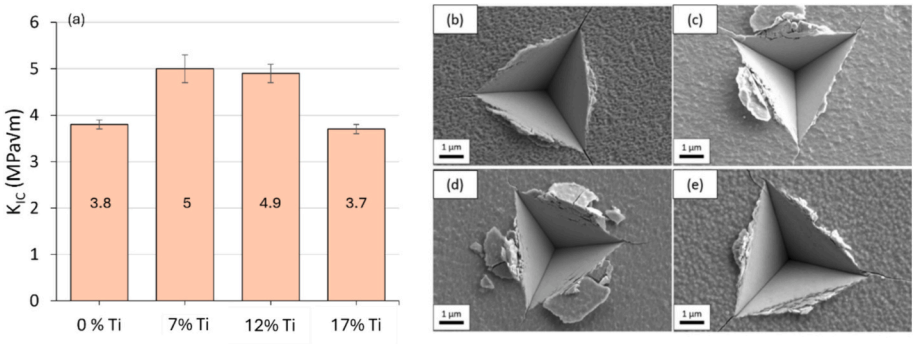

Fig. 6. Results of cube corner indenter nanoindentation toughness measurements with indents of 300 mN loads for samples (a), and indents SEM images of specimens deposited at 400 °C with different Ti addition (b) 0 %; (c) 7 %; (d) 12 %; (e) 17 %.

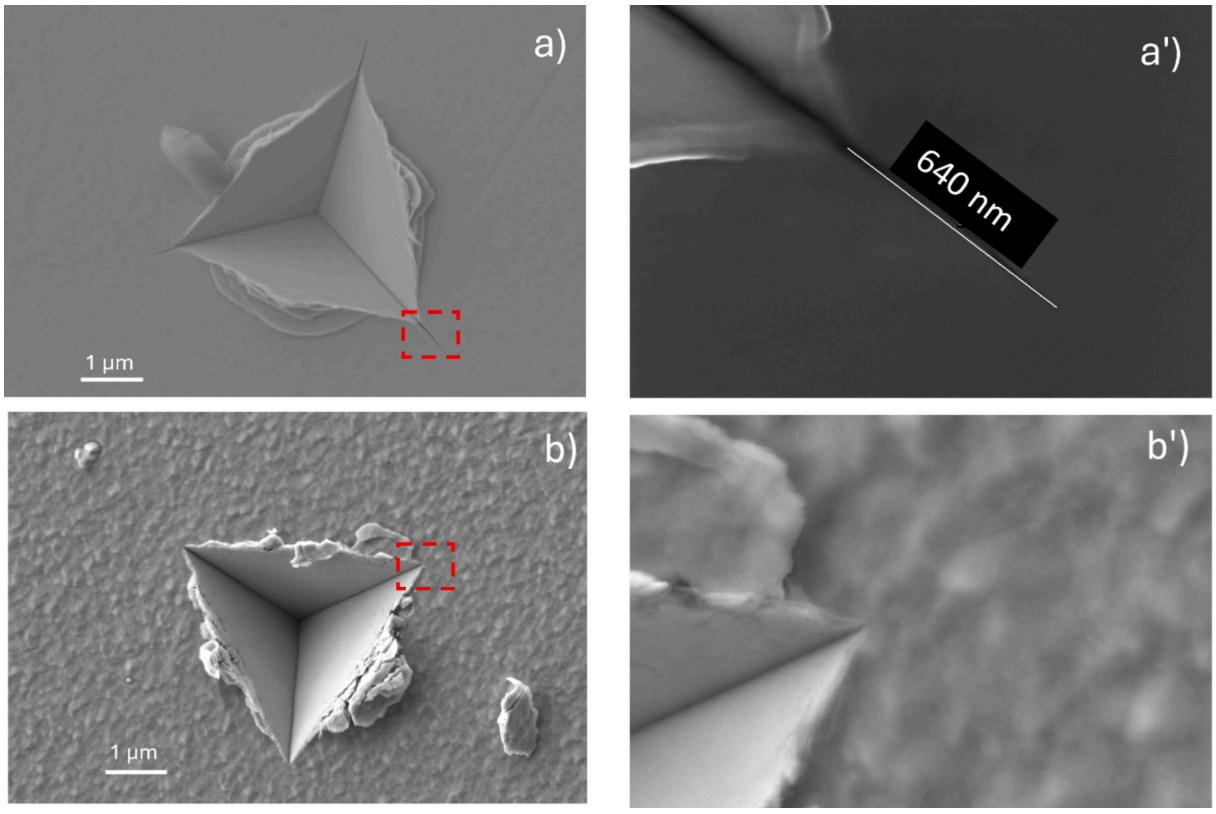

Fig. 7. Results of cube corner indenter nanoindentation toughness measurements with indents of 200 mN loads of 0 % Ti (a, a') and 7 % Ti (b, b'). The magnified area of corner (a', b') is marked with a red rectangle.

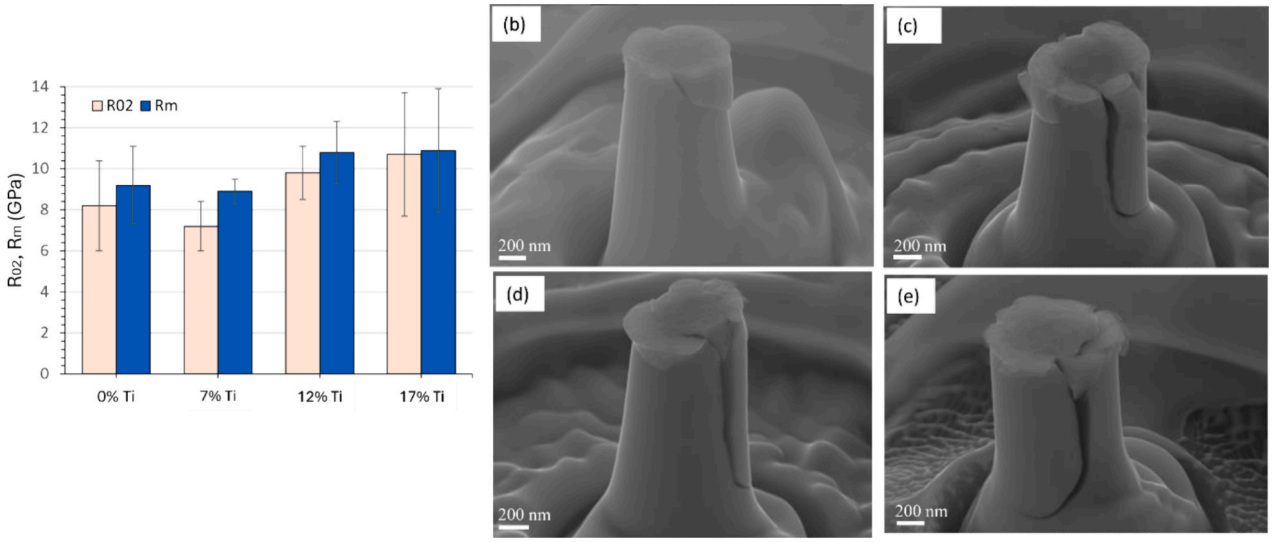

Fig. 8. Results of the 0.2 % offset yield strength ($R_{0.2}$) and ultimate compression strength (R_m) from micro-pillar compression for samples with different Ti content (a), and SEM images of micro-pillars deposited at T_s = 400 °C after compression with the different addition of Ti: (b) 0 %; (c) 7 %; (d) 12 %; (e) 17 %.

was obtained for 7 % titanium ($0.21 \cdot 10^{-6}$ mm^3/Nm) where mechanical studies showed the highest indentation fracture toughness and hardness above 40 GPa. Due to the value of the applied load (two times lower than critical load L_{C3}) and the geometry of the counter sample, the coating wear is abrasive. The microscopic analysis of abrasion effects showed that wear occurs without visible cracking or chipping of the layers.

4. Discussion

Presented in Fig. 2 cross section surfaces show a change of microstructures from partially featureless (Fig. 2a) to columnar with features characteristic of Zone T structural zone model (SZM) [36]. A similar featureless structure of WB_2 was obtained at a surface temperature below 400 °C using DC MS with −50 V bias [37] and RF MS [38]. Typically, at a relatively low temperature, adatoms on a growing surface cannot rearrange completely due to difficulties in surface diffusion.

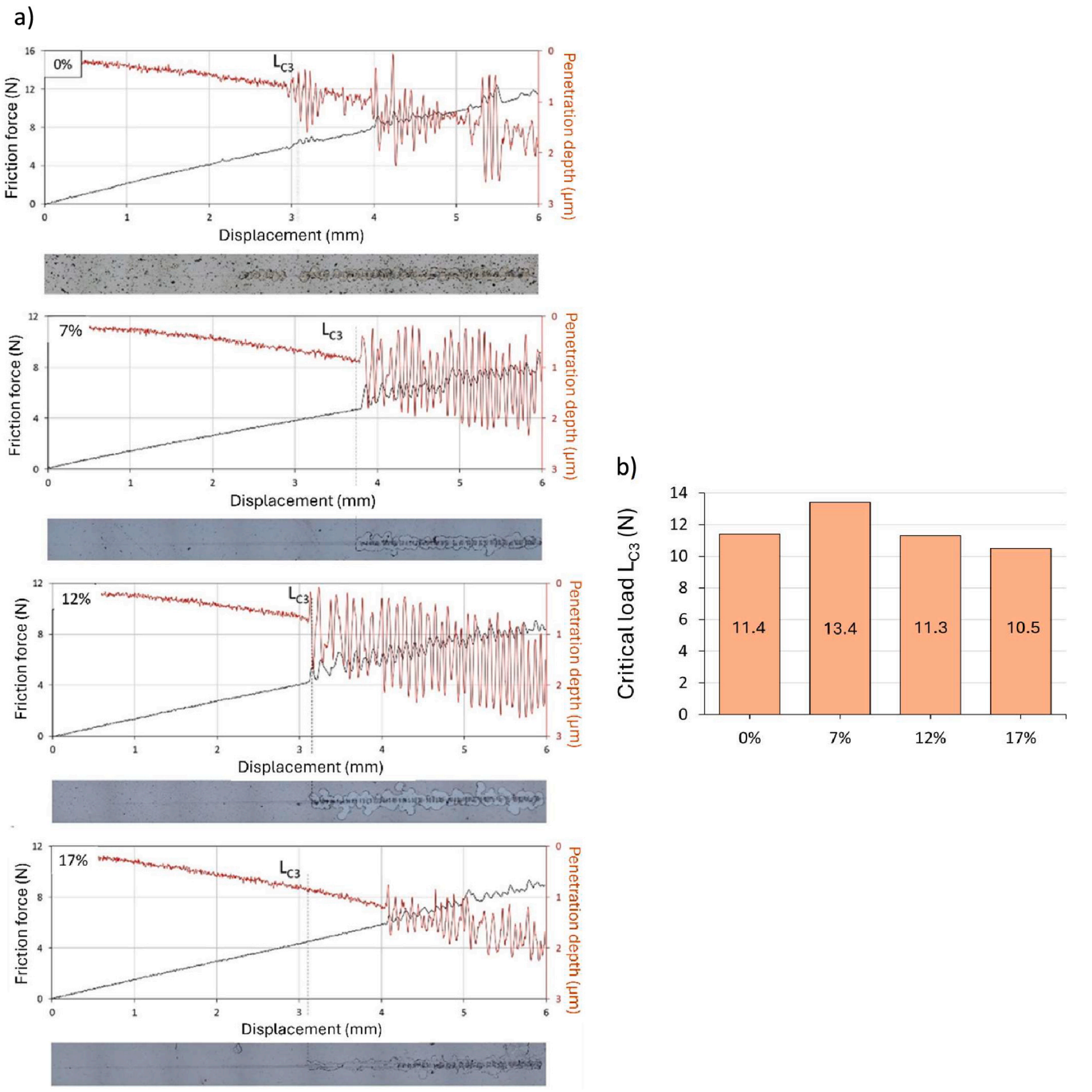

Fig. 9. Representative curves of friction force and penetration depth determined by scratch test, and light microscope images of the surface morphology of the corresponding scratch track for coatings (a) and critical loads L_{C3} of the tested coatings (b) with increasing Ti content (0–17 %); T_s = 400 °C.

Thus, crystallites cannot grow greatly, so an featureless structure develops. In the case of coatings with the addition of titanium, co-deposition of active forms of additional element is difficult to avoid. As X-ray diffraction measurement shows (Fig. 3), both the WB_2 alpha and TiB_2 alpha phases are observed in the deposited layers. As a result of the limited solubility of titanium, its free titanium atoms may constitute an active form of impurities, which, as a result of segregation, may cause the formation of columnar structure. This process can be activated already at a very low, sometimes almost undetectable, concentration of impurities in the incident beam of vapour [27]. An additional factor that promotes the growth of the Zone T structure is the surface diffusion, which should have a considerable value. Such a value is usually obtained for the $0.2 < Ts/Tm < 0.4$ temperature interval. In the case of materials such as WB_2 with very high melting temperatures, surface diffusion can also rise by increasing plasma energy. Such a possibility gives the HiPIMS method. The growth of films using HiPIMS is characterized by high ionic fluxes to the substrate of relatively low energies (several tens of eV) [29]. These growth conditions enhance surface diffusion, leading to film densification. As shown in Fig.4g,h, the obtaining of columnar crystalline structure is possible even in substrate temperature T_s = 300 °C. During magnetron sputtering of tungsten borides, the lighter element is lost due to collision with heavier argon and tungsten [22,39].

It should be noted that loosing of boron is not a disadvantage. The theoretical and experimental studies show that *P6/mmm* tungsten boride polymorph boron vacancies cause an increase in elasticity and even hardness [12,40]. WB_2 *P6/mmm* is a metastable polymorph with

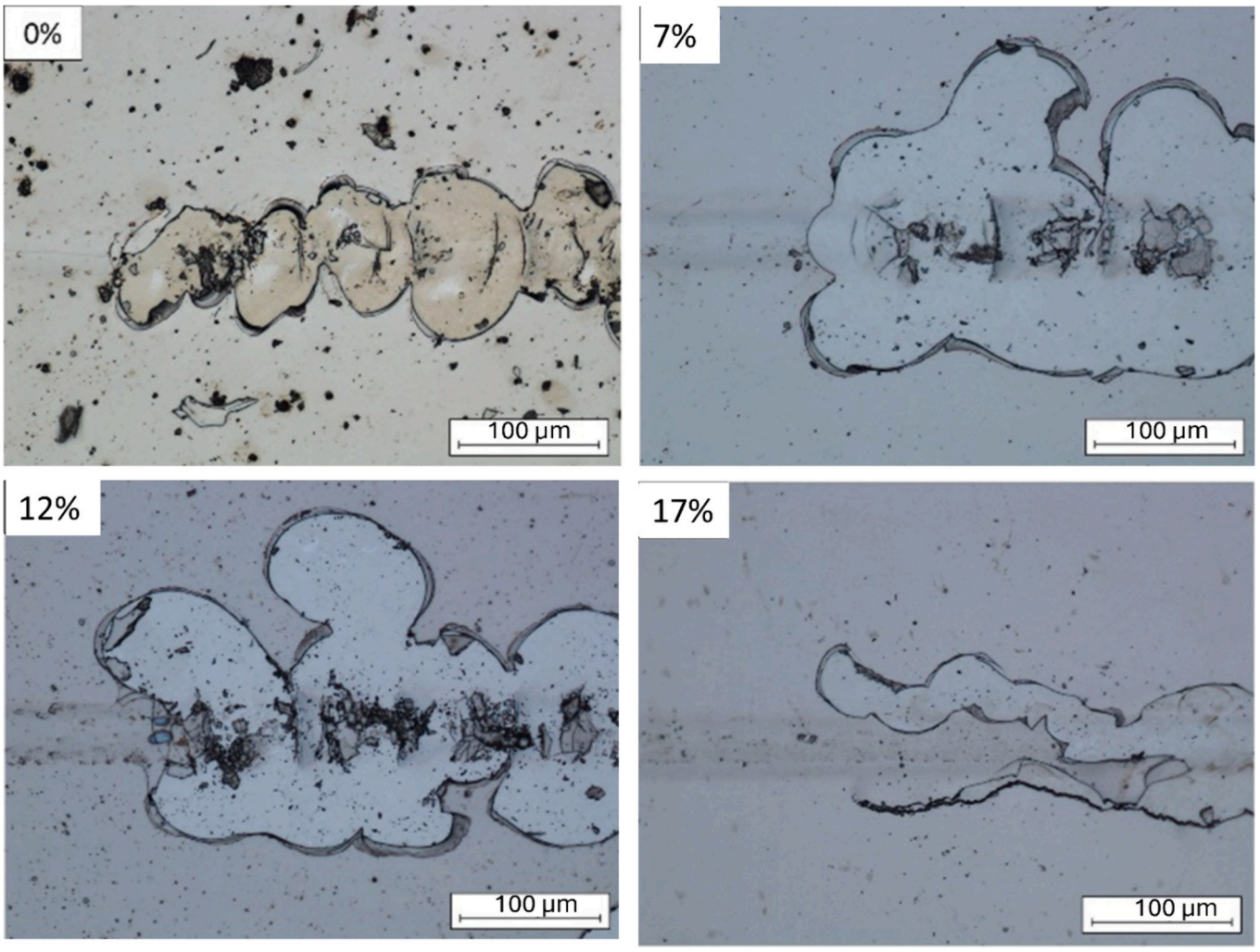

Fig. 10. Initial delamination areas observed during the scratch-testing of W-Ti-B layers with increasing Ti content (0–17 %); T_s = 400 °C.

negative formation energy much lower than $P6_3/mmc$ at stoichiometric composition. The introduction of boron vacancies causes a significant increase of the negative formation energy, and αWB_2 is even more mechanically stable than the ωWB_2 polymorph [18]. Also, the high vacancy concentration and their disordered distribution can improve the deformation ability through effects like unit-cell disturbances that absorb deformation energy, increased valence electron concentration, and hindered dislocation nucleation/motion [40]. Results of mechanical measurements presented in Table 2 indicate the correlations between the microstructure, mechanical properties (the hardness H, the effective Young's modulus E^*, the elastic recovery W_e and stress σ) and the amount of alloying titanium delivered to the growing coating. The change from featureless to crystalline (Zone T) microstructure causes an abrupt increase in deposited films' hardness. At the same time the, Young's modulus grows at the beginning to 430 GPa, but the further increase of titanium amount causes the decrease of this property when hardness is stable. Due to Hooke's law $\sigma = E \cdot \varepsilon$ (where ε is the strain), a decrease of Young's modulus with stable hardness H (σ = const) gives the possibility of higher elastic deformation prior to a failure. Due to a characteristic structure of αWB_2 where the hexagonal-shaped unit cell with alternating stacking of covalently bonded boron hexagons and metal layers, W-Ti-B coatings possess very high hardness. Also, XRD patterns (Fig. 3) show that in higher titanium amounts, two compounds are detected besides tungsten diboride αTiB_2, which is observed and induced by interface hardening due to a dual-phase microstructure. It should be noted that αTiB_2 is much harder than αWB_2 what also increases the hardness of coating. Additionally, calculated from the XRD pattern, the crystallite size is 13–19 nm for 7 % and 17 % of titanium, respectively, which causes the strength of obtained materials to increase due to the Hall-Petch effect.

Introducing vacancies and alloying elements (αTiB_2 is harder but more brittle than αWB_2) increases the mechanical stability and hardness. As it was mentioned above, the vacancies can also decrease the Young's modulus. In a result, a plastic index $H/E^* > 0.1$ was obtained. The ratio H/E^* is proportional to the resistance to wear and the elastic strain ε up to a rupture (failure) of the coating. This means that the higher the ratio of H/E^*, the higher the resistance of the coating to wear and failure [41].

The increase of energy due to HiPIMS deposition and the addition of alloying element titanium at the surface temperature of 400 °C changed the microstructure from featureless to columnar (Fig. 2) and decreased thickness (Table 1). Obtaining a dense and more ordered microstructure causes the residual micro-stress to increase. Applied substrate bias V_s = −50 V causes the W-ion portion of each HIPIMS pulse to be attracted to the substrate and causes the film densification by heavy-ion irradiation (m_W = 183.85 amu versus m_{Ti} = 47.88 amu) while minimizing Ar^+ bombardment and subsequent trapping in interstitial sites [21]. Since W is a film constituent, film stress remains low. The residual stress also influences on the slight shifts to lower angles of the {101}-diffraction peaks (see Fig. 3). The increase of the c-lattice constant with the growth of titanium content correlates to the trend measured for the residual stress with the highest compressive stress. Obtained variable structure on the cross-section, as is the case with the sample with 7 % Ti, which

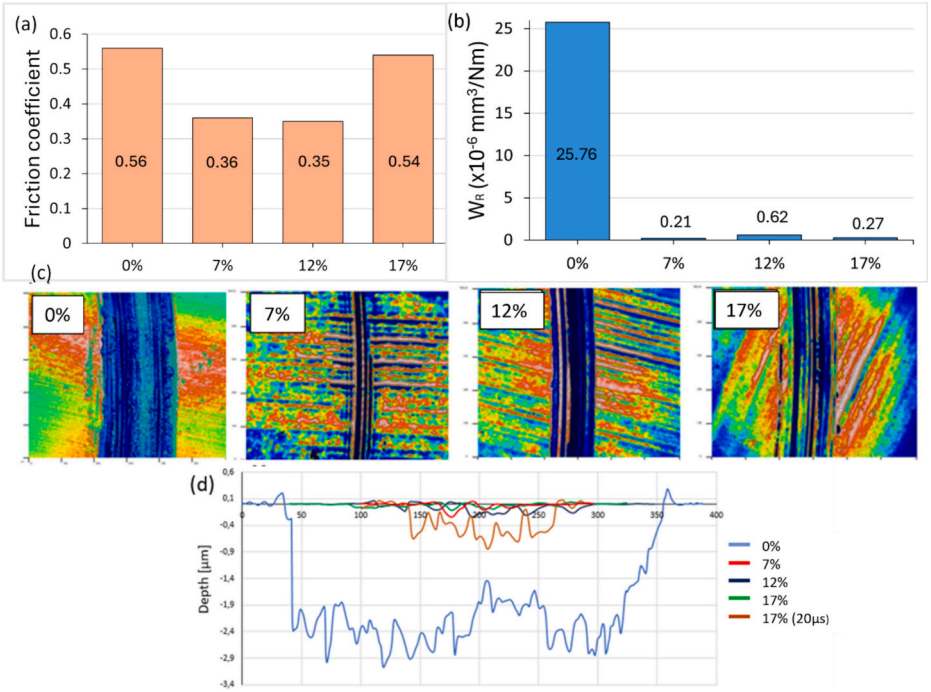

Fig. 11. Friction coefficient (a), wear rate (b), surface morphology (c) and section surface profile of the track (d) after the ball-on-disc wear test of W-Ti-B layers with 0 %, 7 %, 12 % and 17 % of Ti content; T_s = 400 °C.

does not have columnar structure up to the substrate and in the sample with 12 % Ti, which is composed of columnar and "V"-shaped grains near the substrate surface, influences the nanoindentation toughness by adding additional barriers in the way of cracks. The analysis of cracks based on Figs. 6 and 7 may lead to a false conclusion that the film's ductility increases with the titanium increase. As shown in Fig. 6, a load of 300 mN was required to obtain cracks for the film with titanium. At 200 mN, cracks are still not noticeable. However, there is some chipping effect around the indentation. For titanium-free coatings, cracking begins at a load of <100 mN and progresses as the load increases. A comparison of the load-displacement curves (Fig. 12) shows that in both cases (0 and 12 % Ti), the displacement of the indenter is smaller than the film thickness and reaches ~84 % of the layer thickness. Due to the influence of the substrate, the allowable value should be below 50 % to correctly determine K_{Ic}. However, an interesting observation can be made from the indentation curves. For a coating without Ti, the curve is smooth, and it is difficult to find when the foil starts to crack. For 12 % Ti, the curve is more irregular, with faults that may indicate a cracking and spalling effect. At a load of 175 mN, a major excursion is observed, which probably indicates coating damage and increased brittleness.

The micropillars compression curves (Fig. 13) were additionally analyzed to support this conclusion. Specimens with titanium behave like brittle material in which failure occurs immediately after reaching the yield limit (compression strength). Samples without Ti show somewhat intermediate behaviour. For strains just above the elastic limit, cracking is visible but there are no catastrophic failures as with samples with titanium. In the plastic deformation range, cracks are not observed even at high strains. Therefore, it can be concluded that layers without titanium are more ductile. The lack of radial cracks at higher loads for coatings with titanium can be explained by higher compressive stress, no homogeneous compact columnar microstructure, and higher adhesion to the substrate with much lower stiffness.

Fig. 9 shows the course of changes in the friction force, depth under load, acoustic emission and friction coefficient during the scratch test with a linearly variable load from 1 N to 20 N. Delamination of the tested coating occurs in the load range from 10.5 N (24 % Ti) to 13.3 N (8 % Ti). After exceeding the load of 14.3 N, the nature of the observed damage is similar for samples with the addition of titanium - small, separated fragments of the coating with numerous transverse cracks

are observed in the abrasion path. This mechanism indicates the transfer of shear stresses through the layer to the areas in front of the indenter and the delamination of the coating as a result of shear stresses.

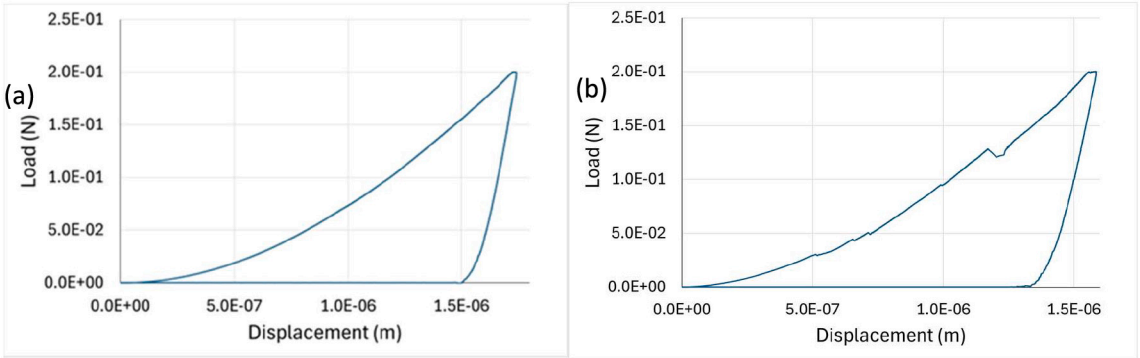

Fig. 12. Load displacement curves of cube corner indentation under load 200 mN of coatings with 0 % (a) and 12 % (b) titanium.

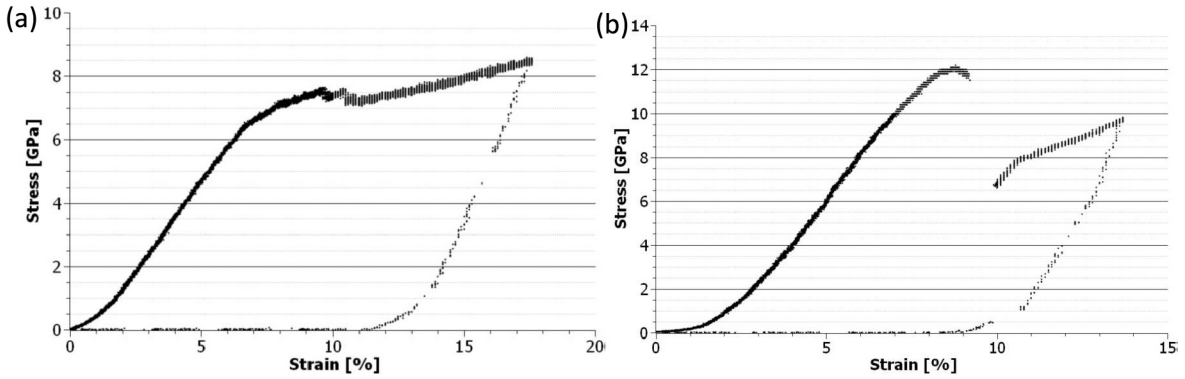

Fig. 13. Compression curves of micropillars with 0 % (a) and 12 % (b) titanium.

This is related to high cohesion of the coating resistance to compression and low resistance to stretching.

According to Fig. 11 it can be seen that the friction properties of WB_{2-z} films improved with the addition of titanium. Coatings with 7 % and 12 % titanium are characterized by exceptional wear resistance with a lower friction coefficient and wear rate (0.21 $\bullet 10^{-6}$ mm^3/Nm) than other films. According to Archard's theory [42], high hardness is responsible for better wear behaviour. Moreover, high *We* and *H/E** and K_{1c} values indicate that the corresponding coatings have high crack resistance. Therefore, in the case of layers with 17 % Ti, where K_{Ic} has the lowest value, the friction coefficient is comparable to WB_{2-z} layers. The compressive stress σ helps to close the cracks formed in the film during the wear process [43]. Finally, the relatively low surface roughness, which is essential in friction behaviour, can also lead to a low coefficient of friction and wear rate. To better understand the mechanisms responsible for the wear resistance of the films, both the depth profile and the worn surface of the wear marks formed on the films were examined, as shown in Fig. 10. The layers show relatively wide (about 200 μm) and shallow wear marks (about 100 nm). In Fig. 10c, no impurities were observed, suggesting no wear due to delamination and cracking of the layers during the test. All wear traces show shallow plough, indicating that abrasive wear is the main type of film damage. During the wear resistance test, the tensile stresses are incorporated into the film. If these stresses exceed adhesion strength, the chipping and delamination start. If we assume that the coatings with titanium have similar mechanical properties, lower adhesion may result in faster delamination and the introduction of impurities that will accelerate layer wear. Because of the low thickness of the deposited films (<2 um), the properties of the substrate can additionally impact the cracking of the film and also wear resistance [41]. The higher the adhesion, the greater the influence of the substrate. However, the most significant influence on wear resistance is incorporated by the change of microstructure and increase of the ratio H/E*. Since films with titanium have a higher H/E* ratio, the resistance to frictional wear is also much higher for these coatings. Additionally, the highest adhesion of film with 7 % Ti causes the highest wear resistance value.

5. Conclusions

Featureless αWB_{2-z} and crystalline $\alpha W_{1-x}Ti_xB_{2-z}$ thin layers were prepared on nitrided steel substrates and Si wafers by High Power Impulse Magnetron Sputtering (HiPIMS). Their structure, residual stresses, mechanical and tribological properties, and adhesion were systematically investigated as a function of the amount of titanium. The effect of titanium content on the films properties obtained from our experimental results can be summarized as follows:

(1) The structure of the $W_{1-x}Ti_xB_{2-z}$ coatings strongly depends on the amount of titanium addition. Films deposited without titanium, even at 400 °C are still featureless. The addition of titanium enables the obtaining of "Zone T" like structures (structural zone diagram) with characteristic "V" shape grains, which although being superhard structures, retain their ductile character and high cracking resistance. A combination of hardness >40 GPa, plastic index >0.11 and elastic recovery >0.63 with compressive stress qualify titanium alloyed αWB_{2-z} coatings to noteworthy groups of "flexible" and superhard materials [34]. During compression of micropillars made of featureless coatings (0 % Ti), the fracture along the slip plane is observed when the addition of titanium causes uniform compression and bulging on the top of the pillar next to the crack initiation along column boundaries.

(2) Using HiPIMS sputtering from a single SPS sintered target decreases the deposition temperature even to 300 °C without microstructure and mechanical properties changes. Layers obtained with this method possess relatively low residual compressive stresses. The stress of alloyed coatings also shows no dependence on the Ti content, and compressive stress σ is less than −0.9 GPa.

(3) After exceeding the solubility limit of titanium (films with 17 % at. Ti), the layers are still superhard, but their nanoindentation toughness decreases, and 0.2 % offset yield strength ($R_{0.2}$) and ultimate compression strength (R_m) increase above 11 GPa. Also, an increase of friction coefficient from 0.35 (12 % Ti) to 0.54 is observed.

(4) The shortening of pulse duration (20 μm), and thus increasing the energy of the material reaching the substrate, improves the mechanical properties. However, the deposited layers are much thinner, resulting in lower abrasive and wear resistance.

(5) This work demonstrates the excellent tribological properties of the WB_{2-z} alloyed with 7 % and 12 % at. titanium layers. However, the highest adhesion is obtained for 7 % of titanium. In all cases, the wear of film has an abrasive character.

Our findings demonstrate the concept of designing and obtaining titanium-alloyed tungsten boride coatings by HiPIMS deposition. The perfect combination of strength and ductility of these new materials has great potential to break the inverse relationship between strength and ductility. In addition, further optimization potential is available through the combination of various strengthening mechanisms resulting from titanium addition and the option to influence surface diffusion by increasing the energy of the incoming target material. Lowering the deposition temperature and limiting the deposition to one magnetron increases the possibility of using the presented solution in many industrial applications.

Funding

This work was funded by the National Centre for Research and

Development (NCBR, Poland) under project no. TECHMATSTRATEGIII/0017/2019 - purchase of a coatings deposition system and microstructure, nanoindentation, wear resistance and adhesion studies; and National Science Centre (NCN, Poland) 2022/47/B/ST8/01296 – mechanical studies (crack resistance, micropillars compression, film stress).

The co-author Jaroslaw J. Jasinski, acknowledges the support from the European Union Horizon 2020 research and innovation program under NOMATEN Teaming grant agreement no. 857470 and from the European Regional Development Fund via the Foundation for Polish Science International Research Agenda Plus program grant no. MAB PLUS/2018/8 which partially covered his salary during the preparation of this article

CRediT authorship contribution statement

Tomasz Mościcki: Writing – original draft, Resources, Project administration, Formal analysis, Data curation, Conceptualization. **Rafał Psiuk:** Writing – review & editing, Investigation, Data curation. **Dariusz Jarząbek:** Writing – review & editing, Methodology, Investigation. **Marta Ciemiorek-Bartkowska:** Investigation, Data curation. **Krzysztof Kulikowski:** Investigation. **Jarosław Jasiński:** Writing – review & editing, Investigation. **Mateusz Włoczewski:** Investigation. **Małgorzata Lewandowska:** Writing – review & editing, Methodology.

Declaration of competing interest

The authors declare that they have no known competing financial interests or personal relationships that could have appeared to influence the work reported in this paper.

Data availability

Data will be made available on request.

References

[1] E. Lotfi-Khojasteh, H. Elmkhah, M. Nouri, P. Mayrhofer, Atomic radius mismatch: a key parameter for design and synthesis of high-entropy physical vapor deposition coatings—review, Adv. Eng. Mater. 26 (2024) 2301934.
[2] J. Marshall, D. Walker, P. Thomas, HRXRD study of the theoretical densities of novel reactive sintered boride candidate neutron shielding materials, Nucl. Mater. Energy 22 (2020) 100732.
[3] O. Ritchie, The conflicts between strength and toughness, Nat. Mater. 10 (2011) 817–822.
[4] W. Sun, C. Bartel, E. Arca, S. Bauers, B. Matthews, B. Orvañanos, B.-R. Chen, M. F. Toney, L. Schelhas, W. Tumas, J. Tate, A. Zakutayev, S. Lany, A. Holder, G. Ceder, A map of the inorganic ternary metal nitrides, Nat. Mater. 18 (2019) 732–739.
[5] J. Wang, Y. Zhou, Recent Progress in theoretical prediction, preparation, and characterization of layered ternary transition-metal carbides, Annu. Rev. Mat. Res. 39 (2009) 415–443.
[6] X. Gu, C. Liu, H. Guo, K. Zhang, C. Chen, Sorting transition-metal diborides: new descriptor for mechanical properties, Acta Mater. 207 (2021) 116685.
[7] V. Moraes, H. Riedl, C. Fuger, P. Polcik, H. Bolvardi, D. Holec, P.H. Mayrhofer, Ab initio inspired design of ternary boride thin films, Sci. Rep. 8 (9288) (2018) 9288.
[8] T. Fiantok, N. Koutná, D. Sangiovanni, M. Mikula, Ceramic transition metal diboride superlattices with improved ductility and fracture toughness screened by ab initio calculations, Sci. Rep. 13 (2023) 12835.
[9] T. Mościcki, J. Chrzanowska-Giżyńska, R. Psiuk, P. Denis, K. Mulewska, Ł. Kurpaska, M. Chmielewski, M. Wiśniewska, D. Garbiec, Thermal and mechanical properties of (W,Zr)B2-z coatings deposited by RF magnetron sputtering method, Int. J. Refract. Met. Hard Mater. 105 (2022) 105811.
[10] C. Fuger, B. Schwartz, T. Wojcik, V. Moraes, M. Weiss, A. Limbeck, C. Macauley, O. Hunold, P. Polcik, D. Primetzhofer, P. Felfer, P. Mayrhofer, H. Riedl, Influence of ta on the oxidation resistance of WB2−z coatings, J. Alloys Compd. 864 (2021) 158121.
[11] B. Bakhit, D.L.J. Engberg, J. Lu, J. Rosen, H. Högberg, L. Hultman, I. Petrov, J. E. Greene, G. Greczynski, Strategy for simultaneously increasing both hardness and toughness in ZrB2-rich Zr1−xTaxBy thin films, J. Vac. Sci. Technol. A 37 (2019).
[12] C. Fuger, V. Moraes, R. Hahn, H. Bolvardi, P. Polcik, H. Riedl, P. Mayrhofer, Influence of Tantalum on phase stability and mechanical properties of WB2, MRS Commun. 9 (1) (2019) 375–380.
[13] B. Bakhit, S. Dorri, A. Kosari, A. Mol, I. Petrov, J. Birch, L. Hultman, G. Greczynski, Microstructure, mechanical, and corrosion properties of Zr1-xCrxBy diboride alloy thin films grown by hybrid high power impulse/DC magnetron co-sputtering, Appl. Surf. Sci. 591 (2022) 153164.
[14] T. Mościcki, R. Psiuk, J. Radziejewska, M. Wiśniewska, D. Garbiec, Properties of spark plasma sintered compacts and magnetron sputtered coatings made from Cr, Mo, Re and Zr alloyed tungsten diboride, Coatings 11 (2021) 1378.
[15] M. Maździarz, R. Psiuk, A. Krawczyńska, M. Lewandowska, T. Mościcki, Effect of zirconium doping on the mechanical properties of W1−xZrxB2 on the basis of first-principles calculations and magnetron sputtered films, Arch. Civ. Mech. Eng. 22 (193) (2022) 1–30.
[16] B. Wicher, O. Pshyk, X. Li, B. Bakhit, V. Rogoz, I. Petrov, L. Hultman, G. Greczynski, Superhard oxidation-resistant Ti1-xAlxBy thin films grown by hybrid HiPIMS/DCMS co-sputtering diboride targets without external substrate heating, Mater. Des. 238 (2024) 112727.
[17] R. Psiuk, M. Milczarek, P. Jenczyk, P. Denis, D. Jarząbek, P. Bazarnik, M. Pisarek, T. Mościcki, Improved mechanical properties of W-Zr-B coatings deposited by hybrid RF magnetron – PLD method, Appl. Surf. Sci. 570 (2021) 151239.
[18] H. Euchner, P. Mayrhofer, H. Riedl, A. Limbeck, P. Polcik, S. Kolozsvari, Solid solution hardening of vacancy stabilized TixW1-xB2, Acta Mater. 101 (2015) 55–61.
[19] O. Sobol, S. Dub, A. Pogrebnjak, R. Mygushchenko, A. Postelnyk, A. Zvyagolsky, G. Tolmachova, The effect of low titanium content on the phase composition, structure, and mechanical properties of magnetron sputtered WB2-TiB2 films, Thin Solid Films 662 (2018) 137–144.
[20] T. Mościcki, R. Psiuk, H. Słomińska, N. Levintant-Zayonts, D. Garbiec, M. Pisarek, P. Bazarnik, S. Nosewicz, J. Chrzanowska-Giżyńska, Influence of overstoichiometric boron and titanium addition on the properties of RF magnetron sputtered tungsten borides, Surf. Coat. Technol. 390 (2020) 125689.
[21] G. Greczynski, I. Petrov, J. Greene, L. Hultman, Paradigm shift in thin-film growth by magnetron sputtering: from gas-ion to metal-ion irradiation of the growing film, J. Vac. Sci. Technol. A 37 (2019) 060801.
[22] J. Chrzanowska-Giżyńska, P. Denis, M. Giżyński, Ł. Kurpaska, I. Mihailescu, C. Ristoscu, Z. Szymański, T. Mościcki, Thin WBx and WyTi1-yBx films deposited by combined magnetron sputtering and pulsed laser deposition technique, Appl. Surf. Sci. 478 (2019) 505–513.
[23] M. Hu, Q. Cao, X. Wang, D. Zhang, J.-Z. Jiang, Fluence-dependent microstructure and nanomechanical property in Co-Ni-V medium entropy alloy thin films, Scr. Mater. 203 (2021) 114050.
[24] A. Anders, Tutorial: reactive high power impulse magnetron sputtering (R-HiPIMS), J. Appl. Phys. 121 (2017) 171101.
[25] F. Zhao, Q. Tao, C. You, M. Ye, L. Li, Y. Han, S. Dong, X. Wang, T. Cui, P. Zhu, Enhanced hardness in tungsten–substituted molybdenum diboride solid solutions by local symmetry reduction, Mater. Chem. Phys. 251 (2020) 123188.
[26] G. Akopov, M. Yeung, C. Turner, R. Mohammadi, R. Kaner, Extrinsic hardening of Superhard tungsten tetraboride alloys with group 4 transition metals, J. Am. Chem. Soc. 138 (17) (2016) 5714–5721.
[27] P. Barna, M. Adamik, Fundamental structure forming phenomena of polycrystalline films and the structure zone models, Thin Solid Films 317 (1998) 27–33.
[28] L. Zauner, R. Hahn, E. Aschauer, T. Wojcik, A. Davydok, O. Hunold, P. Polcik, H. Riedl, Assessing the fracture and fatigue resistance of nanostructured thin films, Acta Mater. 239 (2022) 118260.
[29] J. Greene, Review article: tracing the recorded history of thin-film sputter deposition: from the 1800s to 2017, J. Vac. Sci. Technol. A 35 (2017) (p. 05C204).
[30] B. Bakhit, D. Primetzhofer, E. Pitthan, M. Sortica, E. Ntemou, J. Rosen, L. Hultman, I. Petrov, G. Greczynski, Systematic compositional analysis of sputterdeposited boron-containing thin films, J. Vac. Sci. Technol. A 39 (2021) 063408.
[31] J. Berlin, Analysis of boron with energy dispersive x-ray spectrometry, Imaging Microsc. 13 (2011) 19–21.
[32] B. Lawn, A. Evans, D. Marshall, Elastic/plastic indentation damage in ceramics: the median/radial crack system, J. Am. Ceram. Soc. 63 (1980) 574–581.
[33] D. Harding, W. Oliver, G. Pharr, Cracking during nanoindentation and its use in the measurement of fracture toughness, MRS Proc. 356 (1994) 663.
[34] G. Janssen, M. Abdalla, F. van Keule, B. Pujada, B. van Venrooy, Celebrating the 100th anniversary of the Stoney equation for film stress: developments from polycrystalline steel strips to single crystal silicon wafers, Thin Solid Films 517 (2009) 1858–1867.
[35] J. Musil, Flexible hard nanocomposite coatings, RSC Adv. 5 (2015) 60482.
[36] E. Kusano, Structure-zone modeling of sputter-deposited thin, Appl. Sci. Converg. Technol. 28 (6) (2019) 179–185.
[37] Y. Liu, C. Jiang, Z. Pei, H. Lei, J. Gong, C. Sun, Microstructure and properties of AlB2-type WB2 thin films deposited by direct-current magnetron sputtering, Surf. Coat. Technol. 245 (2014) 108–116.
[38] J. Chrzanowska-Giżyńska, P. Denis, S. Woźniacka, Ł. Kurpaska, Mechanical properties and thermal stability of tungsten boride films deposited by radio frequency magnetron sputtering, Ceram. Int. 44 (2018) 19603–19611.
[39] M. Kroker, P. Soucek, M. Slapanska, V. Sochora, M. Jilek, P. Vasina, Predicting the composition of W-B-C coatings sputtered from industrial cylindrical segmented target, Surf. Coat. Technol. 438 (2022) 12841.
[40] Z. Chen, Y. Huang, N. Koutná, Z. Gao, D. Sangiovanni, S. Fellner, G. Haberfehlner, S. Jin, P. Mayrhofer, G. Kothleitner, Z. Zhang, Largemechanical properties enhancement in ceramics through vacancy-mediated unit cell disturbance, Nat. Commun. 14 (2023) 8387.

[41] J. Musil, Advanced hard nanocomposite coatings with enhanced toughness and resistance to cracking, in: S. Zhang (Ed.), Thin Films and Coatings: Toughening and Toughness Characterization, CRC Press, USA, 2015, pp. 377–463 (chapter 7).
[42] J. Archard, Contact and rubbing of flat surfaces, J. Appl. Phys. 24 (1953) 981–988.
[43] J. Musil, Hard nanocomposite coatings: thermal stability, oxidation resistance and toughness, Surf. Coat. Technol. 207 (2012) 50–65.